



Highly photocatalytic activity of brookite/rutile TiO₂ nanocrystals with semi-embedded structure

Yanfeng Cao^a, Xiaoting Li^a, Zhenfeng Bian^a, Addis Fuhr^b, Dieqing Zhang^{a,**}, Jian Zhu^{a,b,*}

^a Chinese Education Ministry Key Lab of Resource Chemistry and Shanghai Key Laboratory of Rare Earth Functional Materials, Shanghai Normal University, Shanghai 200234, China

^b Chemical & Biomolecular Engineering Department, University of California, Los Angeles, CA 90095, USA

ARTICLE INFO

Article history:

Received 16 April 2015

Received in revised form 29 June 2015

Accepted 5 July 2015

Available online 13 July 2015

Keywords:

Brookite/rutile TiO₂

Semi-embedded structure

Photocatalytic activity

Solvothermal approach

ABSTRACT

A facile solvothermal approach was used to prepare brookite-type TiO₂ nanocrystals with different phase content and structure, accomplished by adjusting the ratio of TiCl₄ to *t*-BuOH. The obtained biphasic brookite/rutile TiO₂ nanocrystals showed a high brookite weight content (72%). The photocatalytic degradation of phenol under UV-irradiation was used to determine the synergetic effect from the combination of different phases (e.g., brookite, anatase, and rutile). The biphasic NST-4 composed of brookite and rutile exhibited the highest degradation rates, with rate constants three times higher than commercial Degussa P-25. Detailed analysis found that, besides phase composition and content, the semi-embedded structure was essential to obtain a superior activity of biphasic TiO₂ samples.

© 2015 Elsevier B.V. All rights reserved.

1. Introduction

As one of the most promising photocatalysts, TiO₂ nanocrystal has received much attention in the past several decades [1–5]. The photocatalytic activity of TiO₂ can be influenced by many factors such as crystal structure, particle size, surface morphology, and porosity [6–11], with crystal structure being the major factor in photocatalytic performance [7,10,12]. Many researchers have discussed the intrinsic connection between crystal phase and photocatalytic activity [13–18]. Of the two most common TiO₂ crystal phases (anatase and rutile), anatase has the greater photoactivity [19]. Not surprisingly, most of the research on TiO₂ photocatalysts has focused on anatase, rutile, and their mixtures [20–25]. In contrast, the brookite phase of TiO₂ has received much less attention. Importantly, this disinterest is not due to the photocatalytic activity of brookite, but rather the thermodynamic meta-stability of brookite [26,27].

The development of modern techniques has made the successful synthesis of brookite-type TiO₂ materials increasingly common.

Kominami et al. successfully synthesized brookite TiO₂ with photocatalytic activity in the mineralization of AcOH to CO₂ equal to that of commercial TiO₂ (Degussa P-25) [28]. Using low-pH, Lin et al. developed a novel preparation of high-quality brookite TiO₂ nanosheets surrounded with four {210}, two {101}, and two {201} facets [29]. These nanosheets exhibited outstanding activity for the degradation of organic contaminants surpassing Degussa P25. These results suggest that brookite TiO₂ has a higher photocatalytic activity than anatase TiO₂. Inspired by these results, much effort has been devoted to construct mixed phase brookite-type TiO₂ with superior photoactivity. For instance, Ozawa et al. reported the synergetic effects of anatase and brookite bi-phasic materials [30]. They found the activities of these mixed-phase materials were 5.4 times greater than that of single-phase materials in the oxidation of CH₃CHO(g). More recently, a bicrystalline anatase-brookite TiO₂ catalyst was used by Zhao et al. in the photoreduction of CO₂ [31]. This anatase rich bicrystalline anatase-brookite TiO₂ showed higher rates of CO production than pure anatase, pure brookite, and commercial Degussa P25. As the brookite-type TiO₂ displays better performance as a photo catalyst, there is a requirement for deep understanding of superior activity on brookite containing TiO₂ materials.

Hydrothermal synthesis under alkaline conditions (e.g., NaOH, Et₃N, and urea) has been the most commonly used route to obtain brookite based TiO₂ materials [31–33]. Conversely, use of the solvothermal method is relatively unexplored. To date, one of the most successful works has employed toluene or acid ethanol.

* Corresponding author at: Chinese Education Ministry Key Lab of Resource Chemistry and Shanghai Key Laboratory of Rare Earth Functional Materials, Shanghai Normal University, Shanghai, 200234, China. Fax: +86 21 64322272.

** Corresponding author.

E-mail addresses: dqzhang@shnu.edu.cn (D. Zhang), jianzhu@shnu.edu.cn (J. Zhu).

Table 1
Structural parameters and activities of NSTi samples.

Sample code	TiCl ₄ /TBA (mol ratio)	Anatase		Brookite		Rutile		S_{BET} (m ² g ^{−1})	Reaction rate constant ^a
		Size _A (nm)	Content _A (w%)	Size _B (nm)	Content _B (w%)	Size _R (nm)	Content _R (w%)		
NSTi-1	0.033	6.5	73	7.8	23	/	4	196	1.02
NSTi-2	0.066	7.5	30	7.9	26	27.9	44	165	1.38
NSTi-3	0.10	7.2	3	9.1	58	13.1	39	105	1.54
NSTi-4	0.16	/	/	9.8	72	10.1	28	100	2.74
NSTi-5	0.25	/	/	9.6	46	10.5	54	103	1.87

^a Reaction rate constant (k , $\times 10^{-2}$ min^{−1}) was calculated from the photocatalytic activity on phenol degradation.

However, they have not been able to surpass brookite content of 35% [16,34]. Due to the high-degree of hydrogen bonding in H₂O, organic solvents used in solvothermal approaches generally have weaker intermolecular interactions than water used in hydrothermal methods. As a result, the higher pressure and lower surface tension in solvothermal processes may result in TiO₂ with a higher crystallinity and larger surface. Based on this conception, we detailed out successfully synthesis of multiphasic TiO₂ materials via a nonhydrolytic solvothermal approach using TiCl₄ and *t*-BuOH with no additional structural agent.

Our primary focus was on the effect of varying the TiCl₄ and *t*-BuOH ratio on the crystal structure and photocatalytic performance of TiO₂. Here, we report the successful synthesis of crystalline TiO₂ with different phases and morphologies. For the first time, bicrystalline TiO₂ materials were prepared with >70% brookite content from this solvothermal method. These brookite/rutile biphasic TiO₂ catalysts exhibited superior photocatalytic activity in the photocatalytic oxidation of phenol in comparison to commercial P-25 TiO₂. Detailed structural analysis revealed that the formation of a semi-embedded structure was key for the synergetic effect between brookite and rutile.

2. Experimental

2.1. Materials

Titanium tetrachloride (TiCl₄) and anhydrous ethanol were purchased from Aladdin. *Tert*-butanol (*t*-BuOH) was purchased from Sigma–Aldrich. All of the chemicals were analytical grade and used directly without further purification.

2.2. Sample preparation

Developing from the previously reported “alkyl halide elimination” route proposed by Arnal et al. [35], the nonhydrolytic solvothermal process was utilized in this study. In a typical preparation, 10 mL TiCl₄ was added dropwise into a vigorously stirred *tert*-butanol solution (50 mL) in a 100 mL round-bottom flask at 30 °C under a flow of argon (20 mL/min). After continuous stirring for 3 h, the resultant gel was aged in a Teflon-lined autoclave at 110 °C for 6 days. The product was centrifuged and washed with ethanol and water to remove the residual Cl[−] and solvent several times, followed by drying in air overnight. Changing the molar ratio of TiCl₄ and *t*-BuOH, different nonhydrolytic solvothermal derived TiO₂ (NSTi) samples were prepared and labeled as NSTi-X (see Table 1), respectively.

2.3. Characterizations

X-ray diffraction (XRD) patterns were recorded on a Bruker D8 Advance X-ray diffractometer with Cu-K α radiation at a scan rate of 0.02° s^{−1}. The phase content of the samples was calculated accord-

ing to the following formula [18],

$$W_A = \frac{K_A A_A}{K_A A_A + K_R A_R + K_B A_B}, W_B = \frac{K_B A_B}{K_A A_A + K_R A_R + K_B A_B},$$

$$W_R = \frac{K_R A_R}{K_A A_A + K_R A_R + K_B A_B}$$

where W_A , W_B and W_R represent the mass fractions of anatase, brookite and rutile, respectively. The A_A , A_B and A_R were the integrated intensity of anatase (1 0 1), brookite (1 2 1) and rutile (1 1 0) peak. The K_A , K_B and K_R were coefficients and their values were 0.886, 2.721 and 1.000, respectively. In two phases contained samples, the coefficient for the absent phase was set to zero. The average crystallite sizes of each phase were determined based on the Scherrer equation using the FWHM data of anatase (1 0 1), brookite (1 2 1) and rutile (1 1 0).

Surface area measurements were carried out on a Micromeritics Tristar 3000 system using N₂ adsorption at 77 K at liquid nitrogen temperature. The specific surface area was determined by the Brunauer–Emmett–Teller (BET) method. Raman spectra were measured on a confocal microprobe Raman system (Super LabRam) at resolution of 1 cm^{−1} by using a He–Ne laser with a wavelength of 632.8 nm as the excitation line. Diffuse reflection (DR) UV–vis spectra were obtained on a Shimadzu UV-2450 Spectrophotometer using BaSO₄ as a reference. Transmission electron micrographs (TEM) was recorded digitally on a JEOL 2011 electron microscope operating at 200 kV with a Gatan slow-scan charge-coupled device (CCD) camera. Photocurrents were measured using an electrochemical analyzer (CHI660D Instruments) in a standard three-electrode system using the prepared samples as the working electrodes with an active area of ca. 20 × 20 mm², a Pt piece as the counter electrode with area of 20 × 20 mm², and saturated calomel electrode as a reference electrode. A 0.50 M Na₂SO₄ aqueous solution was used as the electrolyte. Bias voltage was 0.30 V (Vs. SCE). A 3 W LED UV lamp served as light source with the wavelength about 365 ± 10 nm.

2.4. Photocatalysis test

The photocatalytic activity of TiO₂ samples for the liquid-phase oxidation of 56 mg/L phenol solution was tested on a self-made recirculating photoreactor with a volume of 150 mL at 25 ± 0.5 °C. Artificial UV light (310 nm, 4 × 8 W lamp) was used as irradiation source. The light was initiated after continuing stirring 0.05 g catalysts for about 30 min in phenol solution to achieve the adsorption/desorption equilibrium. And HPLC system (Shimadzu LC-10ATvp) was used to measure the residual organic concentration. Blank experiments (without any catalyst or no light performed) were also made and showed only less than 5% phenol decomposed after reaction for 90 min. A 300 W Xe lamp (Perfect-light, PLS-SXE300) with filter (wavelength was limited in the range from 365 nm to 400 nm) was used as irradiation source to degrade 50 mL methylene blue (MB, 10 mg/L) or rhodamine B (RhB, 20 mg/L)

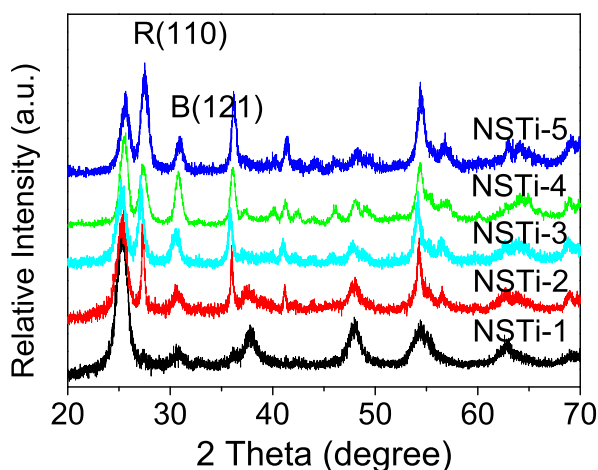


Fig. 1. XRD patterns of NSTi samples.

solution. The concentration of MB and RhB were measured by a UV–vis spectrophotometer (Shimadzu, UV-2450).

3. Results and discussion

3.1. Structure and morphology analysis

The crystalline structures of obtained NSTi samples are shown in Fig. 1. All samples show characteristic peaks at $2\theta = 30.8^\circ$, ascribing to crystal face (1 2 1) of brookite; anatase and rutile are also observed in Fig. 1. The concentration of TiCl_4 in the initial precursor solution greatly influences the formation of TiO_2 crystals with different phases. The increase of TiCl_4 induces an interesting crystalline phase transition from anatase/brookite to rutile/brookite as shown in the samples from NSTi-1 to NSTi-5.

In order to gain insight into the detailed phase composition, a numerical deconvolution technique was used to separate the anatase (1 0 1) peak, the brookite (1 2 0), and the brookite (1 1 n1) peaks at the very narrow 2θ range from 25° to 27° . In accordance with the reference provided, we set up two boundary conditions [36]. (1) The same peak broadening of all diffraction peaks was ascribed to brookite. (2) The intensity ratio of (1 2 0) to (1 1 1) peaks is in proportion to that in JCPDS card (No. 29-1360). Fig. 2 illustrates the fitting analysis of NSTi-1 and NSTi-4. It clearly shows that NSTi-1 is mainly composed of anatase and brookite, while NSTi-4 contains only brookite and rutile. The detailed phase content of all NSTi sam-

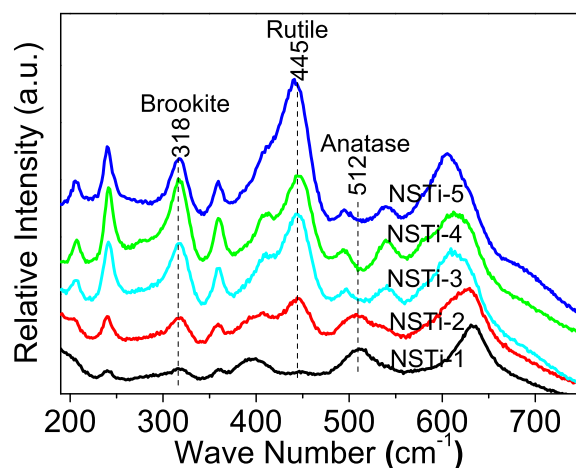


Fig. 3. Raman spectroscopy of NSTi samples.

ples is shown in Table 1. Apparently, the anatase content reduces quickly with the increase in TiCl_4 concentration. No anatase is found in NSTi-4 and NSTi-5. On the contrary, the brookite content gradually increases and arrives at the maximum of about 72% in NSTi-4, followed by a decrease to 46% in NSTi-5. For rutile content, a drastic increase is observed initially. Then it slowly decreases to 28% in NSTi-4. Finally, the rutile content in NSTi-5 increases again to 54%.

The changes in phase composition are always accompanied with the altering of crystal size. The accurate crystal size calculated from FWHM data of anatase (1 0 1), brookite (1 2 1), and rutile (1 1 0) was listed in Table 1. From NSTi-1 to NSTi-3, the anatase and brookite show little increase in crystal size. The crystal size of rutile greatly decreases from 27.9 nm in NSTi-2 to 10.5 nm in NSTi-5. Such variations in crystal size for each phase implies a different crystal growth mechanism caused by the change of concentration of TiCl_4 . The possible explanations are discussed below.

To make a further investigation on the structure, Raman spectroscopy was used to distinguish three polymorphs of TiO_2 (anatase, brookite and rutile). Raman spectroscopy is a surface-sensitive characterization and may display a clearer result than XRD patterns. The bands located at 318, 445 and 512 cm^{-1} in Fig. 3 are well defined and can be attributed to brookite, rutile, and anatase, respectively [37–39]. No anatase is found in NSTi-3, NSTi-4 and NSTi-5. This result is quite consistent with the above XRD results. The absorption band located at 318 cm^{-1} shows the change of brookite content with the increase of TiCl_4 concentration. The

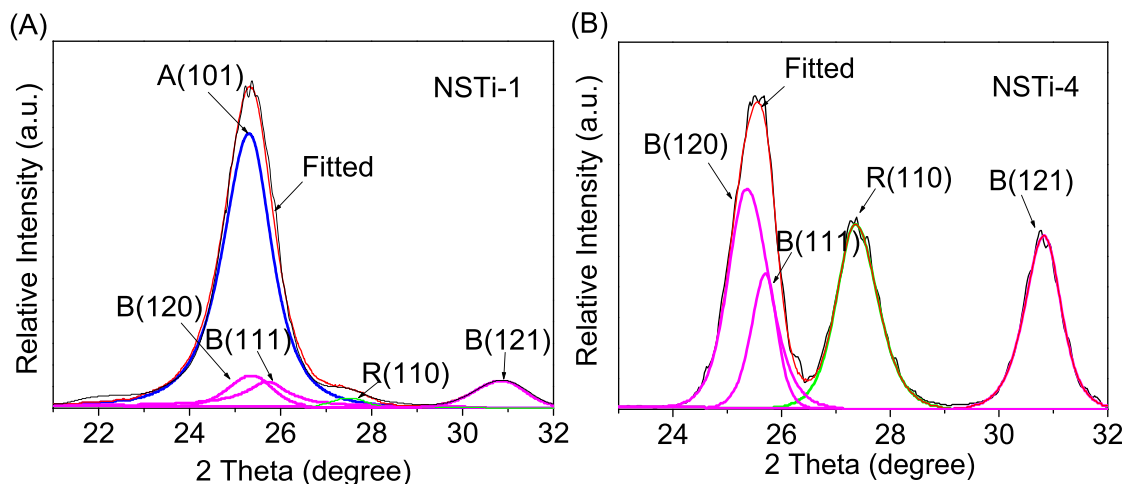


Fig. 2. XRD pattern fitting analysis of sample (A) NSTi-1 and (B) NSTi-4.

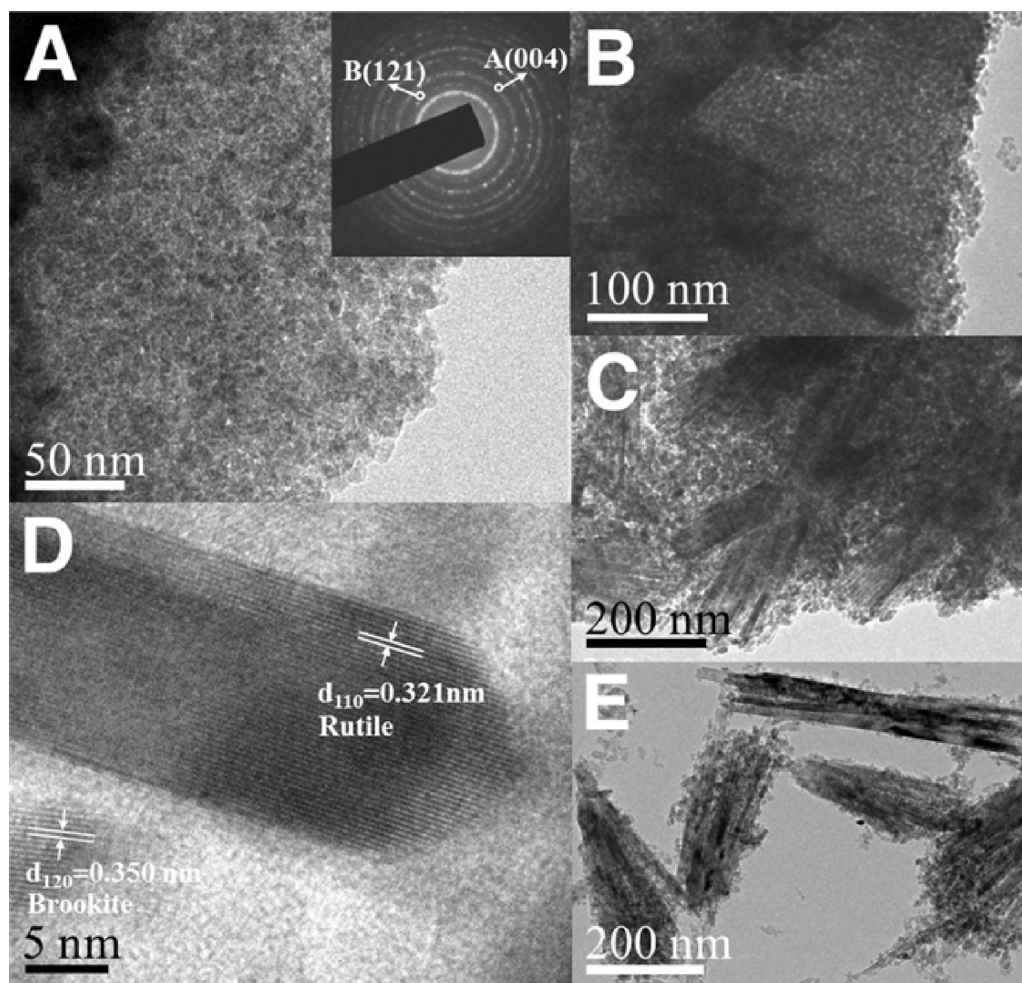


Fig. 4. TEM images of NSTi samples. (A) NSTi-1, (B) NSTi-3, (C) NSTi-4, (D) HRTEM image of NSTi-4, (E) NSTi-5. Inset shows the SAED patterns.

strongest band is found in NSTi-4 meaning the highest amount of brookite, in line with the above XRD results. Deeper insight reveals that only a relatively weak band at 445 cm^{-1} ascribing to rutile is observed in NSTi-2; this differs from the high amount of rutile phase ($\sim 44\%$) calculated from XRD pattern. To explain this difference, we semi-qualitatively compared phase content according to the relative peak intensity, bearing in mind that the Raman spectra were carried out at the same condition. Comparing NSTi-4, NSTi-3, and NSTi-2, the ratio of intensity at 318 cm^{-1} (I_{318}) is 1.28:1.00:0.415. In XRD results, the ratio of brookite content in these three samples is 1.24:1.00:0.448 (72:58:26). The ratio of I_{318} from Raman spectra agrees well with the ratio of brookite content from XRD pattern. However, in the case of rutile, we observed an obvious difference from these two characterizations. The ratio of $I_{445}(\text{NSTi-4}/\text{NSTi-3}/\text{NSTi-2})$ from Raman spectra has been calculated to be 0.915:1.00:0.497. The XRD results show a ratio of rutile content in NSTi-4, NSTi-3, and NSTi-2 for 0.718:1.00:1.13 to be 28:39:44. It seems the rutile contents in NSTi-2 and NSTi-3 are both smaller in the calculation obtained by the Raman method, especially in NSTi-2. These contradictory observations may be due to inhomogeneity of the material surface as compared to the bulk materials [40]. Typically, Raman is effective in characterizing the surface structure and XRD in detecting bulk structure. Therefore, the weak Raman signal of rutile in NSTi-2 and NSTi-3 may come from the special embedded structure. Specifically, the rutile phase is embedded in the interior of the anatase phase. As we focus on the anatase content, a similar phenomenon is also observed in NSTi-1 and NSTi-2. The Raman sig-

nal at 512 cm^{-1} ascribing to anatase does not drastically decrease from NSTi-1 to NSTi-2. But the XRD results show obvious decrease of anatase content from 73% to 30%. This serves as further evidence that most of the anatase forms on the outside of NSTi-2. If we assume the existence of the embedded structure in NSTi-2, it is easy to understand the different results obtained from the Raman spectra and XRD pattern. Following TEM was used to confirm this hypothesis.

Fig. 4 shows the TEM images of NSTi series. The NSTi-1 (Fig. 4A) is composed of nanoparticles with the size around 5 to 8 nm. The inset of Fig. 4A shows selective area electron diffraction (SAED) displaying the high crystallinity of the sample. The diffraction rings of anatase (004) and brookite (121) can be marked, indicating the existence of anatase and brookite. No rutile (110) can be clearly marked. We also could not distinguish the anatase phase from the brookite phase due to the similar interplanar spacing. Similar to NSTi-1, NSTi-3 is also mainly composed of nanoparticles. However, some obscure matrices are found fully embedded in many of the nanoparticles. Clearer images are presented in Fig. 4C and Fig. 4D. In NSTi-4, the nanorod matrices are not full embedded in the nanoparticles, dissimilar to that observed in NSTi-3. From Fig. 4D, the high resolution TEM (HRTEM) images illustrate that the matrices are composed of single crystal nanorods. The observed interplanar spacing of approximately 0.321 nm can be ascribed to the rutile (110) facet. In the case of the brookite phase, the round nanocrystal shows interplanar spacing around 0.350 nm, ascribing to the brookite (120) facet. In NSTi-5 (Fig. 4E), the number

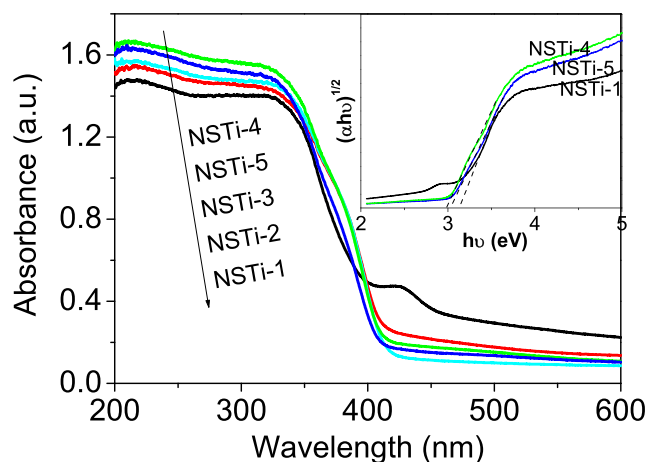


Fig. 5. UV-vis absorption spectra of NSTi samples.

of nanoparticles are drastically reduced and the morphology of nanorod matrices can be seen clearly due to the significant increase in the amount of rutile from 28% to 54%. From the TEM images we observe the embedded structure with inner rutile nanorod matrices and outer anatase/brookite nanoparticles. The above hypothesis of embedded structure from XRD and Raman analysis has been confirmed by the TEM images.

The formation of NSTi samples with different structure is illustrated in Scheme 1. The mol ratio of TiCl_4 to $t\text{-BuOH}$ greatly influences the nucleation and growing process as well as the final structure of NSTi samples. Under low concentration of TiCl_4 , anatase and brookite crystals form small spheres (in NSTi-1). Anatase takes precedence over brookite resulting in an anatase-dominated system. Increasing the TiCl_4 content is beneficial for the crystal yield in the case of NSTi-2. Increasing the quantity of nanocrystals results in increased aggregation; this further induces the formation of rutile at the interface of the interconnected anatase crystals. A similar mechanism for the transition of anatase to rutile was reported by others [41,42]. The inner rutile crystals are most likely embedded in the anatase crystals, especially when rutile particles present nanorod morphology. Brookite becomes the dominant phase after further increase in TiCl_4 (NSTi-3 and NSTi-4). It is mentioned that $t\text{-BuOH}$ was also important in the formation of the brookite crystals. When we replaced the $t\text{-BuOH}$ with ethanol or benzyl alcohol, only anatase was found. The high concentration of intermediate product (Ti-OBu) under low pH may relate to the formation of brookite. In sample NSTi-5, more rutile nanorods are finally detected due to the highest thermal stability of rutile among the three common phases of TiO_2 .

3.2. UV-vis and photocatalytic performance

The UV-vis absorption spectra of NSTi samples were shown in Fig. 5. All of samples show absorption in UV region due to the intrinsic band gap of TiO_2 . The NSTi-4 displays the strongest absorption at wavelengths (λ) shorter than 350 nm. The NSTi-2, NSTi-3, and NSTi-4 samples appear at a similar absorption edge, while the NSTi-5 and NSTi-1 experiences a slight shift toward shorter wavelengths. The inset of Fig. 5 gives the optical band edge of NSTi-1, NSTi-4, and NSTi-5 using Kubelka-Munk conversion. The observed band gaps for these samples are 3.12 eV (NSTi-1), 2.97 eV (NSTi-4), and 3.03 eV (NSTi-5), respectively. Due to the unique band structure of each crystal phase, the three samples exhibit different band gaps, which may induce the synergetic effect.

The photocatalytic degradation of phenol was used as a model reaction to evaluate photocatalytic activities of the present NSTi

catalysts (Fig. 6). Commercial Degussa P-25 powders served as a control. All NSTi samples display much higher photocatalytic activities than Degussa P-25. NSTi-4 sample exhibits the highest catalytic activity. According to the reported work [43,44], photocatalytic degradation of phenol on TiO_2 is a first-order reaction. In order to compare the activities of different NSTi samples in detail, we plotted the $\log C/C_0$ with irradiation time to calculate reaction rate constant (k) (Fig. 6B). The result shows that the calculated k of NSTi-4 sample is $2.74 \times 10^{-2} \text{ min}^{-1}$, that is three times as high as that of commercial P-25 ($0.89 \times 10^{-2} \text{ min}^{-1}$). To investigate potential applications of NSTi samples in environmental remediation, other dyes such as methylene blue (MB) and rhodamine B (RhB) were also chosen as target organic pollutants. Fig. 7 shows that NSTi-4 has the highest photocatalytic activity on the degradation of both MB and RhB. Under the first 30 mins, the removal rate of NSTi-4 for MB and RhB were 82 and 86%, respectively. Under the same condition, the Degussa P-25 displays only 18 and 72%. On the degradation of above three different pollutants (phenol, MB and RhB), the similar tendency was observed that was NSTi-4 > NSTi-5 > NSTi-1.

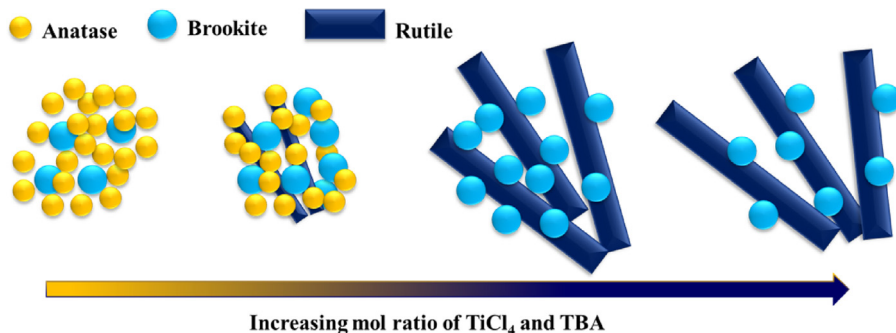
3.3. Discussion about photocatalytic activities

Comparing the different NSTi samples with each other, it was a surprising discovery to find that NSTi-1 possesses both the highest BET surface area, and the lowest activity (shown in Table 1). It seems surface area plays a trivial role in deciding the final activity. Further comparing NSTi-1, NSTi-2, and NSTi-3, we found that the activities were not reduced with the decrease of surface area. The NSTi-3, NSTi-4, and NSTi-5 have similar surface area, but display notably different activities. This phenomenon differs from the previous work using acetone(g) as a reactant, which reported that the surface area was important for the final activity [45]. This contrasting opinion may be due to the fact that the reported case is a gas-solid reaction. In our case, we are dealing with a liquid-solid system. As a result, surface area is not a dominant factor.

Taking into consideration the possible influence of the hybrid crystal structure on the photocatalytic activities, we analyzed the relationship between k and phase content (Fig. 8). The changes of k and the brookite content demonstrate a similar tendency. It may imply the important role of brookite in influencing the final activity. However, it is still difficult to explain the observed experimental fact that NSTi-2 and NSTi-3 have low activities. It is believed that the synergetic effect between different crystal phases is the main factor. There are three ways to influence the synergetic effect here.

(1) Different phase composition. NSTi-2 shows a higher activity than NSTi-1. The NSTi-2 displays the similar content of brookite as NSTi-1. The main differences between the two samples are the content of anatase and rutile. Despite the trace of rutile, NSTi-1 is mainly composed of anatase and brookite. NSTi-2 is composed of anatase, rutile and brookite, but with low content of anatase. The synergetic effect among rutile and brookite may become more efficient in the separation of photo-generated electrons and holes than between anatase and brookite. With the increase of brookite content, the synergetic effect between rutile and brookite is enhanced; thus, resulting in the increase of activity of NSTi-3. The photocurrent test was performed to see the intrinsic separation of photo-generated electron/hole on the different NSTi samples. Fig. 9 confirms that NSTi-3 shows higher current density than NSTi-2 and NSTi-1.

(2) Proportion of different phases. In our cases, NSTi-4 (72% brookite, 28% rutile) and NSTi-5 (46% brookite, 54% rutile) have the same phase composition (just brookite and rutile), but with different phase proportion. The activity of NSTi-5 is obviously lower than that of NSTi-4. It shows that the proper proportion of brookite and rutile is required to achieve a superior photocatalytic activity. According to this rule, NSTi-3 (58% brookite, 39% rutile) may have



Scheme 1. Illustration of formation of NSTi samples with different structures.

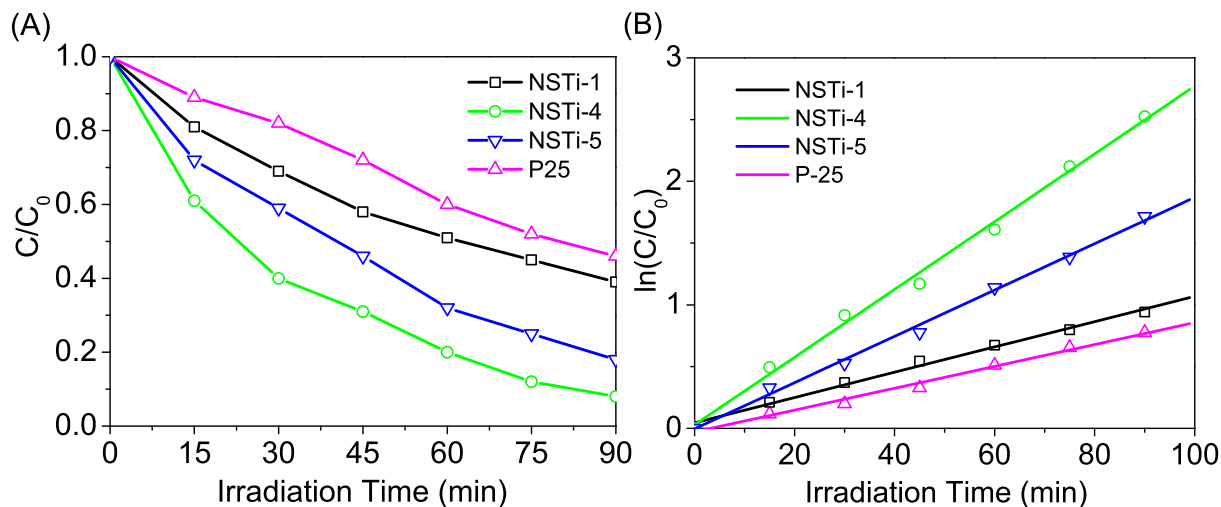


Fig. 6. Photocatalytic activities of NSTi samples for degrading phenol (56 mg/L). (A) C/C_0 Vs irradiation time. (B) $\ln(C/C_0)$ Vs irradiation time.

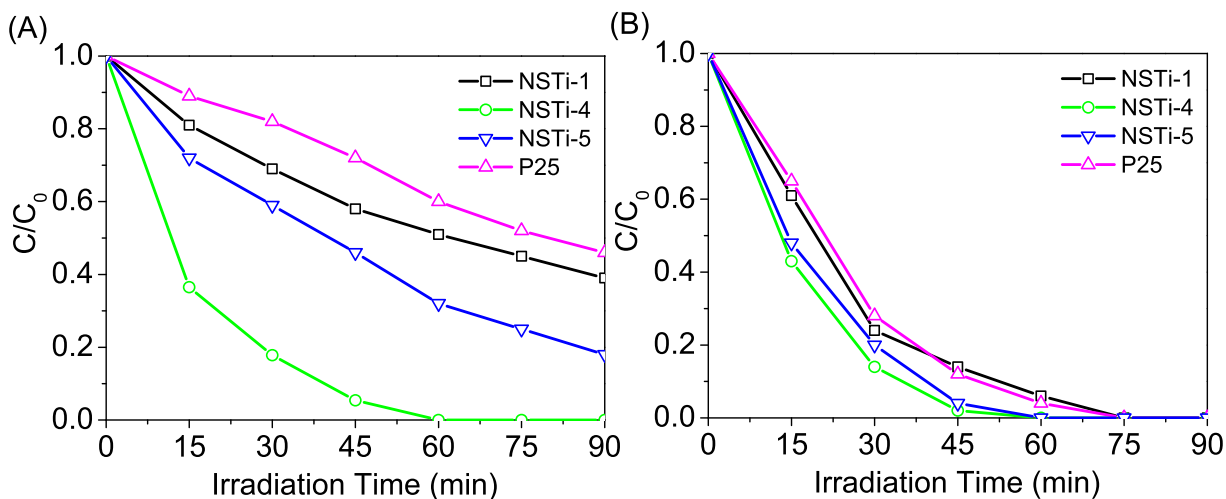


Fig. 7. Photocatalytic activities of NSTi samples for degrading (A) MB (10 mg/L) and (B) RhB (20 mg/L).

higher activity than NSTi-5. However, the opposite is true. Therefore, there must be some other factors that influence the synergetic effect.

(3) Different morphology and hybrid crystal structure. This factor has rarely been discussed in the work relating to synergetic effect. In NSTi-4, the rutile is as a form of nanorod matrix made by directional growth of single crystal rutile. Such rod-like single crystal may improve charge transport and suppress charge recombination. ¹⁶ Brookite nanocrystals show sphere morphology. The

nanorod matrices are surrounded by brookite spheres to form the embedded structure. Based on this structure, it is probably easier to transfer charge carriers between the brookite and rutile. On the other hand, the hybrid crystal structure is also important. If the nanorod matrices are fully imbedded, more light will be absorbed by outside brookite spheres. This will result in a low excitation of inner rutile. If this happens, the synergetic effect between brookite spheres and rutile matrices will be restricted. Therefore, when NSTi-2 and NSTi-3 have a higher content of outside brookite

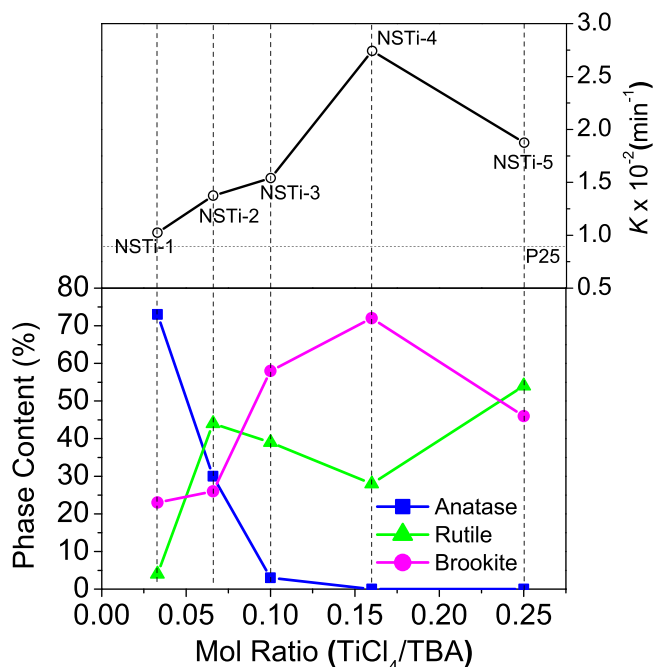


Fig. 8. Effect of mol ratio of TiCl₄ and TBA on K (blank circle) and phase content (filled square-anatase, filled triangle-rutile and filled circle-brookite).

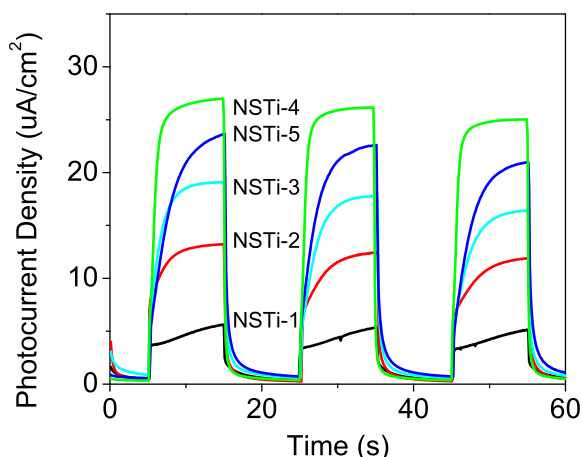


Fig. 9. Photocurrent responses in light on-off process under visible-light irradiation ($\lambda = 365 \pm 10$ nm).

sphere, there appears to be a lower activity than NSTi-4 and NSTi-5 with a semi-embedded structure. The change of photocurrent densities in Fig. 9 also confirms the more effective separation of photo-generated carriers of NSTi-4 and NSTi-5 than NSTi-2 and NSTi-3.

Above all, NSTi-4 shows the highest activity. The main reason is that bicrystalline NSTi-4 has a semi-embedded structure with optimized proportion of brookite and rutile.

4. Conclusion

In conclusion, a series of brookite based TiO₂ samples were successfully obtained by a facile solvothermal method. The samples' morphology and structure are greatly changed by varying the ratio of TiCl₄ to *t*-BuOH. The NSTi-4 composed with 72% brookite and 28% rutile shows the highest activity in photodegradation of phenol. The brookite/rutile semi-embedded bicrystal structure together with

optimized phase proportion is responsible for the efficient synergistic effect relating to the highest activity of NSTi-4.

Acknowledgements

This material is based upon work supported by the NSF of China (21207090, 21377088, 21477079, 21407106), Shanghai Government (12nm0504000, 13ZR1430600, 14ZZ126, 14ZR1430800), Program from Huo Yingdong Education Foundation (142022), Program for Changjiang Scholars and Innovative Research Team in University (PCSIRT, IRT1269), Program for Professor of Special Appointment (Eastern Scholar, 2012-82, 2013-57), and Doctoral Program of Higher Education (20123127120009).

References

- [1] X.B. Chen, S.S. Mao, Chem. Rev. 107 (2007) 2891.
- [2] M.R. Hoffmann, S.T. Martin, W.Y. Chen, D.W. Bahnemann, Chem. Rev. 95 (1995) 69.
- [3] A. Fujishima, T.N. Rao, D.A. Tryk, J. Photochem. Photobiol. C 1 (2000) 1.
- [4] S.S. Li, C.P. Chang, C.C. Lin, Y.Y. Lin, C.H. Chang, J.R. Yang, M.W. Chu, C.W. Chen, J. Am. Chem. Soc. 133 (2011) 11614.
- [5] Z.Q. Sun, J.H. Kim, Y. Zhao, F. Bijarbooneh, V. Malgras, Y.M. Lee, Y.M. Kang, S.X. Dou, J. Am. Chem. Soc. 133 (2011) 19314.
- [6] K. Tomita, V. Petrykin, M. Kobayashi, M. Shiro, M. Yoshimura, M. Kakihana, Angew. Chem. Int. Ed. 45 (2006) 2378.
- [7] J. Zhu, Z.F. Bian, J. Ren, Y.M. Liu, Y. Cao, H.X. Li, W.L. Dai, H.Y. He, K.N. Fan, Catal. Commun. 8 (2007) 971.
- [8] H.X. Li, Z.F. Bian, J. Zhu, Y.N. Huo, H. Li, Y.F. Lu, J. Am. Chem. Soc. 129 (2007) 4538.
- [9] H.G. Yang, G. Liu, S.Z. Qiao, C.H. Sun, Y.G. Jin, S.C. Smith, J. Zou, H.M. Cheng, G.Q. Lu, J. Am. Chem. Soc. 131 (2009) 4078.
- [10] Z.F. Bian, J. Zhu, J. Wen, F.L. Cao, Y.N. Huo, X.F. Qian, Y. Cao, M.Q. Shen, H.X. Li, Y.F. Lu, Angew. Chem. Int. Ed. 50 (2011) 1105.
- [11] J.B. Joo, Q. Zhang, I. Lee, M. Dahl, F. Zaera, Y.D. Yin, Adv. Funct. Mater. 22 (2012) 166.
- [12] S. Bakardjieva, V. Stengl, L. Szatmary, J. Subrt, J. Lukac, N. Murafa, D. Niznansky, K. Cizek, J. Jirkovskyc, N. Petrova, J. Mater. Chem. 16 (2006) 1709.
- [13] Q.H. Zhang, L. Gao, J.K. Guo, Appl. Catal. B 26 (2000) 207.
- [14] A. Bojinova, R. Kralchevska, I. Poullos, C. Dushkin, Mater. Chem. Phys. 106 (2007) 187.
- [15] L.A. Gu, J.Y. Wang, H. Cheng, Y.C. Du, Chem. Commun. 48 (2012) 6978.
- [16] Y.L. Liao, W.X. Que, Q.Y. Jia, Y.C. He, J. Zhang, P. Zhong, J. Mater. Chem. 22 (2012) 7937.
- [17] Y.B. Luan, L.Q. Jing, Q.Q. Meng, H. Nan, P. Luan, M.Z. Xie, Y.J. Feng, J. Phys. Chem. C 116 (2012) 17094.
- [18] A. Testino, I.R. Bellobono, V. Buscaglia, C. Canevali, M. D'Arienzo, S. Polizzi, R. Scotti, F. Morazzoni, J. Am. Chem. Soc. 129 (2007) 3564.
- [19] J. Zhu, J. Yang, Z.F. Bian, J. Ren, Y.M. Liu, Y. Cao, H.X. Li, H.Y. He, K.N. Fan, Appl. Catal. B 76 (2007) 82.
- [20] T. Meulen, A. Mattson, L. Osterlund, J. Catal. 251 (2007) 131.
- [21] D.L. Jiang, S.Q. Zhang, H.J. Zhao, Environ. Sci. Technol. 41 (2007) 303.
- [22] L. Chen, J. Zhu, Y.M. Liu, Y. Cao, H.X. Li, H.Y. He, W.L. Dai, K.N. Fan, J. Mol. Catal. A 255 (2006) 260.
- [23] R. Su, R. Bechstein, L. Sø, R.T. Vang, M. Sillassen, B. Esbjörnsson, A. Palmqvist, F. Besenbacher, J. Phys. Chem. C 115 (2011) 24287.
- [24] G. Liu, X.X. Yan, Z.G. Chen, X.W. Wang, L.Z. Wang, G.Q. Lu, H.M. Cheng, J. Mater. Chem. 19 (2009) 6590.
- [25] J.S. Yang, W.P. Liao, J.J. Wu, ACS Appl. Mater. Interfaces 5 (2013) 7425.
- [26] Q.X. Deng, M.D. Wei, X.K. Ding, L.L. Jiang, B.H. Ye, K.M. Wei, Chem. Commun. (31) (2008) 3657.
- [27] R. Buonsanti, V. Grillo, E. Carlino, C. Giannini, T. Kipp, R. Cingolani, P.D. Cozzoli, J. Am. Chem. Soc. 130 (2008) 11223.
- [28] H. Kominami, Y. Ishii, M. Kohna, S. Konishia, Y. Kera, B. Ohtanic, Catal. Lett. 91 (2003) 4.
- [29] H.F. Lin, L.P. Li, M.L. Zhao, X.S. Huang, X.M. Chen, G.S. Li, R.C. Yu, J. Am. Chem. Soc. 134 (2012) 8328.
- [30] T. Ozawa, M. Iwasaki, H. Tada, T. Akita, K. Tanaka, S. Ito, J. Colloid Interfaces Sci. 281 (2005) 510.
- [31] H.L. Zhao, L.J. Liu, J.M. Andino, Y. Li, J. Mater. Chem. A 1 (2013) 8209.
- [32] B. Zhao, L. Lin, D.N. He, J. Mater. Chem. A 1 (2013) 1659.
- [33] H. Xu, L.Z. Zhang, J. Phys. Chem. C 113 (2009) 1785.
- [34] G. Li, K.A. Gray, Chem. Mater. 19 (2007) 1143.
- [35] P. Arnal, R.J.P. Corriu, D. Lecelerq, P.H. Mutin, A. Vioux, Chem. Mater. 9 (1997) 694.
- [36] H. Zhang, J.F. Banfield, J. Phys. Chem. B 104 (2000) 3481.
- [37] M. Kobayashi, V.V. Petrykin, M. Kakihana, Chem. Mater. 19 (2007) 5373.
- [38] J.G. Li, T. Ishigaki, X.D. Sun, J. Phys. Chem. C 111 (2007) 4969.
- [39] Y. Hu, H.L. Tsai, C.L. Huang, J. Eur. Ceram. Soc. 23 (2003) 691.
- [40] J. Zhang, M.J. Li, Z.C. Feng, J. Chen, C. Li, J. Phys. Chem. B 110 (2006) 927.

- [41] J.Y. Shi, J. Chen, Z.C. Feng, T. Chen, Y.X. Lian, X.L. Wang, C. Li, J. Phys. Chem. C 111 (2007) 693.
- [42] F.J. Knorr, D. Zhang, J.L. McHale, Langmuir 23 (2007) 8686.
- [43] S. Chatterjee, S. Sarkar, S.N. Bhattacharyya, J. Photochem. Photobiol. A 81 (1994) 199.
- [44] N. Wang, Z.F. Chen, L.H. Zhu, X. Jiang, B. Lv, H.Q. Tang, J. Photochem. Photobiol. A 191 (2007) 193.
- [45] Y. Yu, J.C. Yu, J.G. Yu, Y.C. Kwok, Y.K. Che, J.C. Zhao, L. Ding, W.K. Ge, P.K. Wong, Appl. Catal. A 289 (2005) 186.